TU Delft

Delft University of Technology

Integrated photonics interferometric interrogator for a ring-resonator ultrasound sensor

Ouyang, Boling; Haverdings, Michael; Horsten, Roland; Kruidhof, Marten; Kat, Pim; Caro, Jacob

DOI
10.1364/OE.27.023408

Publication date
2019

Document Version
Final published version

Published in
Optics Express

Citation (APA)
Ouyang, B., Haverdings, M., Horsten, R., Kruidhof, M., Kat, P., & Caro, J. (2019). Integrated photonics interferometric interrogator for a ring-resonator ultrasound sensor. *Optics Express*, *27*(16), 23408-23421. https://doi.org/10.1364/OE.27.023408

Important note
To cite this publication, please use the final published version (if applicable).
Please check the document version above.

Copyright
Other than for strictly personal use, it is not permitted to download, forward or distribute the text or part of it, without the consent of the author(s) and/or copyright holder(s), unless the work is under an open content license such as Creative Commons.

Takedown policy
Please contact us and provide details if you believe this document breaches copyrights.
We will remove access to the work immediately and investigate your claim.

This work is downloaded from Delft University of Technology.
For technical reasons the number of authors shown on this cover page is limited to a maximum of 10.

Research Article | Vol. 27, No. 16 | 5 Aug 2019 | OPTICS EXPRESS 23408

Optics EXPRESS

Integrated photonics interferometric interrogator for a ring-resonator ultrasound sensor

BOLING OUYANG,[1,*] MICHAEL HAVERDINGS,[2] ROLAND HORSTEN,[1] MARTEN KRUIDHOF,[1] PIM KAT,[2] AND JACOB CARO[1]

[1]*Department of Imaging Physics, Delft University of Technology, Lorentzweg 1, 2628 CJ Delft, The Netherlands*
[2]*Technobis tft-fos, Pyrietstraat 2, 1812 SC Alkmaar, The Netherlands*
[*]*B.Ouyang@tudelft.nl*

Abstract: We present a compact integrated photonics interrogator for a ring-resonator (RR) ultrasound sensor, the so-called MediGator. The MediGator consists of a special light source and an InP Mach-Zehnder interferometer (MZI) with a 3×3 multi-mode interferometer. Miniaturization of the MZI to chip size enables high temperature stability and negligible signal drift. The light source has a -3 dB bandwidth of 1.5 nm, a power density of 9 dBm/nm and a tuning range of 5.7 nm, providing sufficient signal level and robust alignment for the RR sensor. The mathematical procedure of interrogation is presented, leading to the optimum MZI design. We measure the frequency response of the sensor using the MediGator, giving a resonance frequency of 0.995 MHz. Further, high interrogation performance is demonstrated at the RR resonance frequency for an ultrasound pressure range of 1.47 – 442.4 Pa, which yields very good linearity between the pressure and the resulting modulation amplitude of the RR resonance wavelength. The measured signal time traces match well with calculated results. Linear fitting of the pressure data gives a sensor sensitivity of 77.2 fm/Pa. The MediGator provides a low detection limit, temperature robustness and a large measurement range for interrogating the RR ultrasound sensor.

Published by The Optical Society under the terms of the Creative Commons Attribution 4.0 License. Further distribution of this work must maintain attribution to the author(s) and the published article's title, journal citation, and DOI.

1. Introduction

Integrated photonics sensors are contributing to many fields, including chemical sensing [1–4], temperature sensing [5, 6], and ultrasound detection [7, 8]. Recently, such sensors for detecting ultrasound based on ring resonators (RRs) fabricated in silicon-on-insulator (SOI) and polymer platforms have attracted attention [9–11], in view of their high sensitivity, small footprint, possibility of realizing a sensor array on chip, immunity to electromagnetic interference and mass producibility. Therefore, high quality interrogation of this type of sensors becomes crucial for their further development and applications.

RR sensors are often interrogated using an optical spectrum analyzer (OSA), for measuring the shift of the transmission spectrum [5, 12]. However, its resolution is limited to the pm range and the interrogation speed is low, which makes an OSA unsuitable for sensing narrow and fast periodic signals. An on-chip arrayed waveguide grating was developed for interrogating a RR gas sensor [13]. The arrayed waveguide grating is suitable for high speed, but its resolution is also too low for RR ultrasound sensors. Another method is the so-called modulation method, using a narrow linewidth tunable laser and a high speed photodetector [9–11]. By placing the laser wavelength at the linear flank of a RR resonance and measuring the resulting modulation of the transmitted power, the resonance-wavelength modulation can be extracted. However, the highest modulation amplitude measurable with this method is limited by the narrow width of a resonance, implying a short flank [9]. In [14] we demonstrate an interrogator for a RR ultrasound sensor

#368610 https://doi.org/10.1364/OE.27.023408
Journal © 2019 Received 3 Jun 2019; revised 19 Jul 2019; accepted 20 Jul 2019; published 31 Jul 2019

Optics EXPRESS

based on a fiber Mach-Zehnder interferometer (MZI) with a 3×3 fiber coupler. Owing to the 3×3 coupler, at least two outputs of the MZI are non-zero for any operation wavelength, enabling detecting a resonance-wavelength modulation resulting from a 1.2 Pa ultrasound pressure [14]. However, due to the large footprint of the fiber circuit, the environmental phase drift of the MZI is hard to control, thus making this fiber interrogator unsuited for long-time measurements. In addition, it requires pre-measurement at high ultrasound pressure for a circle fitting procedure with the measured signals, adding complexity in using the fiber interrogator [14].

Here, as the next step in the development started in [14], we present a compact integrated photonics interrogator, consisting of a photonic integrated circuit (PIC) and a special light source. The PIC includes an integrated photonics MZI with a 3×3 multi-mode interferometer (MMI) and three photodetectors. With this miniaturization of the MZI, the temperature of the MZI can be well controlled during interrogation. Therefore, this new interrogator is very suitable for long-time measurements as well. Similar MZIs have been reported for interrogating fiber Bragg grating (FBG) sensors [15], but not for the RR sensors, which are challenging due to the multiple resonances, the limited control of the resonance wavelength, the narrow resonance linewidth and the low transmission of the fiber-to-RR coupling. We developed a novel light source to overcome these issues. The light source comprises a pump laser, an Er-doped fiber and a tunable FBG. It provides a spectrum with high power density, large tuning range and suitable bandwidth. These properties ensure a high S/N ratio of the output signals, a robust alignment of the source to the sensor, and a large measurement range. By taking into account instrumental offsets stably present in the acquired signals, we avoid the above-mentioned circle fitting and thus strongly simplify the interrogation procedure. We analytically present the interrogation procedure and experimentally demonstrate a low detection limit and a large measurement range of this interrogator. Together with the RR sensor, this integrated interrogator is very promising for medical applications, such as intravascular ultrasound imaging [16]. Therefore, we call this interrogator MediGator (medical interrogator).

2. Ring-resonator ultrasound sensor and MediGator design

2.1. Ring-resonator ultrasound sensor

Here we provide the background of the operation of the RR ultrasound sensor used in the interrogation experiments and present its main characteristics. The latter serve as input for developing the interrogation procedure and for matching of the MediGator and the RR sensor presented in Section 3.

The sensor is very similar to the ones we used in our previous work [14]. It comprises a racetrack-shaped silicon RR located on a silicon dioxide membrane that has its vibrational mode in the MHz range. A difference is that the present sensor has a square membrane, while the previous ones had a circular membrane. Further, the racetrack is parallel to the <100> direction instead of the <110> direction. This gives a somewhat smaller resonance-wavelength shift in response to the applied strain [17]. A schematic of the sensor, a cross-section of the membrane region and a microscope image of the membrane are presented in Figs. 1(a)-1(c). RRs of the type shown in Fig. 1(c) were fabricated at IMEC through the ePIXfab MPW service [18] on a CMOS compatible SOI platform [220 nm Si layer, 2 µm buried oxide (BOX) layer]. The two directional couplers of the RR are identical. The realized waveguide width of the RR is 400 nm. Operational ultrasound sensors result from post-processing in the Kavli Nanolab Delft and subsequent packaging, using the same procedures as described in [7]. The truncated pyramidal hole under the membrane [Fig. 1(b)] is formed in a KOH etch, applied to locally remove the silicon substrate under the RR, using the BOX layer as etch stop. As can be seen in Fig. 1(c), the 84 µm × 84 µm membrane is well aligned to the RR.

In the underwater sensing situation, the membrane's vibrational mode is excited by acoustic waves of proper characteristics. The membrane vibrations induce time-periodic strain in the RR.

Optics EXPRESS

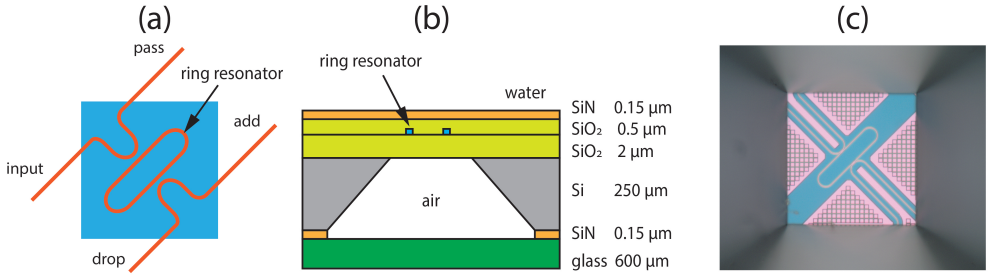

Fig. 1. (a) Schematic of the RR ultrasound sensor: a RR on a square membrane (blue). (b) Cross-section of the membrane region, showing the various layers and their thickness. Membrane thickness is 2.65 µm. A glass platelet seals the air cavity under the membrane. (c) Microscope image of the membrane with the RR, taken from below. Membrane size is 84 µm × 84 µm.

This results in a modulation of the circumference L of the ring and the effective index n_e of the ring's waveguide [17,19]. These quantities determine the resonance condition $n_e(\lambda_r)L = m\lambda_r$ (m is an integer), for which the ring resonates at resonance wavelength λ_r. Thus, the acoustic waves induce a modulation of the resonance wavelength of a magnitude proportional to the pressure of the waves. By interrogating the sensor, the resonance-wavelength modulation can be obtained. This yields information of the incident waves that is required for acoustic imaging applications.

The RR sensor is packaged for measuring the transmission at the drop port, implying that sensing uses a resonance peak instead of a dip. This strongly simplifies the analytical description of the output interrogation signals. The transmission to the drop port of our sensor with identical directional couplers can be expressed as [20]

$$T_{\text{drop}}(\theta) = \frac{\left(1 - r^2\right) a}{1 - 2r^2 a \cos\theta + \left(r^2 a\right)^2}, \tag{1}$$

where r and a are the self-coupling coefficient and single round-trip amplitude transmission, respectively. θ is the accumulated phase of the circulating mode for a single round trip in the ring. Following the same line of reasoning as in [14] for a resonance dip, it can be shown that Eq. (1) for wavelengths λ close to λ_r, i.e., at or close to resonance, can be approximated by

$$T_{\text{drop}}(\lambda) \approx \frac{\varepsilon}{1 + \frac{(\lambda - \lambda_r)^2}{(\gamma_r/2)^2}}. \tag{2}$$

Here ε and γ_r are defined by, respectively

$$\varepsilon = \frac{\left(1 - r^2\right)^2 a}{\left(1 - r^2 a\right)^2}, \tag{3}$$

$$\gamma_r = \frac{\lambda_r^2 \left(1 - r^2 a\right)}{\pi n_g L r \sqrt{a}}. \tag{4}$$

The line shape of the transmission peak given by Eq. (2) is Lorentzian. ε is the maximum transmission value. γ_r is the full width at half maximum (FWHM) of the transmission peak. Obtained from characterization results, our RR sensors typically have $\gamma_r \approx 100$ pm. The free spectral range of the RRs [FSR, with FSR = $\lambda_r^2/(n_g L)$; n_g is the group index] is about 5 nm.

Optics EXPRESS

2.2. MediGator design

The MediGator comprises two main parts: the light source and the InP PIC. In interrogating the RR sensor, the light source is coupled to the input port of the RR, and the drop port of the RR is coupled to the input of the PIC. A schematic of the MediGator is shown in Fig. 2.

The light source is designed to have a high power density, a proper bandwidth and a tuning range exceeding the FSR of the RR. A high power density is needed for sufficient S/N ratio of the MediGator output signals, in view of the narrow RR resonance peak and transmission losses in the system, which is mainly due to fiber-chip connections. The light-source bandwidth should be large compared to γ_r and to the amplitude of the resonance-wavelength modulation resulting from acoustic waves. Further, it should be small compared to the FSR of the RR to enable selecting only a single resonance from the sensor transmission spectrum by tuning the position of the source spectrum. The requirement for the tuning range results from the limited control of the resonance wavelength due to the fabrication variations. A tuning range exceeding the FSR always allows centering the light-source spectrum at a resonance peak.

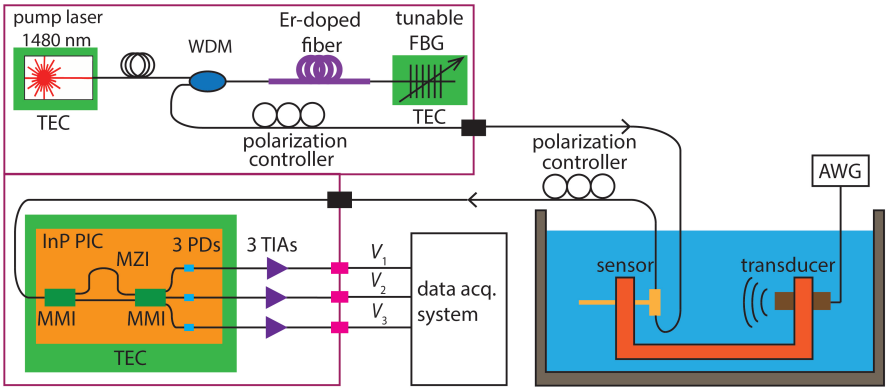

Fig. 2. MediGator (left) and experimental setup (right). The MediGator comprises the tunable light source of high brightness (upper part) and the photonic integrated circuit of MZI and PDs (lower part). Each PD is connected to a TIA. (TEC, thermoelectric cooling; WDM, wavelength division multiplexer; FBG, fiber Bragg grating; PIC, photonic integrated circuit; PD, photodetector; TIA, trans-impedance amplifier; AWG, arbitrary waveform generator; MMI, multi-mode interferometer)

In more detail, the source has similarities with the Er-doped fiber lasers studied in [21]. Here, however, we use light amplification based on a dual-pass configuration instead of a real cavity (see Fig. 2). The source is based on a 1480 nm Fabry-Perot pump laser (Anritsu, AF4B125EA75L) with an internal thermoelectric cooler (TEC). The pump laser is operated in continuous mode. Its light is coupled into an Er-doped fiber [Fibercore I-25 (980/125), length 3.5 m] using a wavelength division multiplexer (WDM, Thorlabs, WD1450B). The 1480 nm light excites the Er ions, which partly decay by spontaneous emission. The spontaneously emitted light in turn leads to stimulated emission by excited Er ions. Part of the fiber-guided spontaneously emitted spectrum reaches a tunable FBG (AtGrating, chirped type, 10 mm long). The FBG reflects the spectrum back into the fiber, where it induces further stimulated emission. As a result, a high brightness spectrum dominated by stimulated emission and of a bandwidth determined by the FBG reflection is coupled out from the fiber via the WDM. By stretching the FBG, the spectral position is tunable. The FBG is chosen to have a bandwidth large enough compared to γ_r of the transmission peak, to ensure that the peak remains within the source spectrum, even for high

modulation amplitudes. After the WDM the light passes a polarization controller for setting the polarization in the optimum direction for the grating coupler of the RR, which is designed for TE polarization. For further stability of the source, the temperature of the pump laser and the FBG are also TEC regulated.

The InP PIC of the MediGator was fabricated at SMART Photonics [22]. It is designed as an MZI with a 2×2 MMI input, a 3×3 MMI output, and three photodetectors with a responsivity of 0.85 A/W for the light of wavelengths between 1520 and 1570 nm (see Fig. 2). In operating the MediGator, at least two of the three outputs of the 3×3 MMI are non-zero. This enables measuring very small phase changes when interrogating the sensor, as will become apparent in Section 5.2. Since the chip of the PIC is very small (4 mm × 4.6 mm), its temperature can be properly stabilized using a TEC, on which the PIC is mounted. Thus, environmental phase drift of the MZI, an issue for the fiber interrogator [14], is virtually absent. Each photodetector output is connected to a trans-impedance amplifier (TIA, Analog Devices, ADA4899-1) with a gain of 2.2 kV/A. Assuming there is no loss, the power transmission $T_{\mathrm{MZI},i}$ $(i = 1, 2, 3)$ to the i^{th} output of the 3×3 MMI is given by

$$T_{\mathrm{MZI},i}(\lambda) = \frac{1}{3}\left[p + q\cos\left(\frac{2\pi}{\lambda}\mathrm{OPD} + \varphi_i + \varphi_e\right)\right] \approx \frac{1}{3}\left[p + q\cos\left(\frac{2\pi}{\mathrm{FSR}}\lambda + \varphi_i + \psi_e\right)\right]. \quad (5)$$

In the ideal case $p = q = 1$, implying a fringe visibility q/p of unity as well. OPD is the optical path-length difference between the MZI arms. The phases φ_i, with $\varphi_i = 0°, 120°$ and $240°(i = 1, 2, 3)$, are the standard phases of the outputs of a 3×3 MMI. φ_e is a phase offset due to imperfections of the MZI and environmental influences, respectively. By Taylor expanding $1/\lambda$ around λ_r and only retaining the first order term, we arrive at the right side of Eq. (5). The FSR of the MZI equals λ_r^2/OPD. ψ_e is defined as $-\varphi_e - 4\pi\mathrm{OPD}/\lambda_r$.

3. Interrogation procedure and matching of the MediGator and the ring-resonator sensor

3.1. Interrogation procedure

Using Eqs. (2) and (5) for the transmission of the RR and MZI, we calculate the MediGator outputs. For incident sinusoidal ultrasound waves of frequency f_0, the resonance-wavelength modulation is written as $\widetilde{\delta\lambda_r}(t) = \delta_0 \sin(2\pi f_0 t)$, where δ_0 is the resonance-wavelength modulation amplitude. We rewrite Eq. (2) as

$$T_{\mathrm{drop}}\left(\lambda, \widetilde{\delta\lambda_r}(t)\right) = \frac{\varepsilon}{1 + \frac{\left(\lambda - \lambda_r - \widetilde{\delta\lambda_r}(t)\right)^2}{(\gamma_r/2)^2}}. \quad (6)$$

Following the flow of the signals in Fig. 2 and using the integrating property of the photodetectors, the output of the three TIAs can be written as

$$V_i(\widetilde{\delta\lambda_r}(t)) = \alpha P_{LS} R_{ph} G \int_0^\infty T_{\mathrm{drop}}\left(\lambda, \widetilde{\delta\lambda_r}(t)\right) T_{\mathrm{MZI},i}(\lambda) d\lambda. \quad (7)$$

Here α represents the wavelength independent overall transmission coefficient of components other than the RR and the MZI between the light source and photodetector. P_{LS} is the power density of the light source. Because γ_r is more than one order smaller than the FBG bandwidth and δ_0 in practice is below 50 pm, we approximate the light-source spectrum as a constant. R_{ph} is the responsivity of the photodetector and G is the gain of the TIAs.

We calculate the integral in Eq. (7) by contour integration in the complex plane, using the residue theorem, to arrive at V_i given by:

$$V_i\left(\widetilde{\delta\lambda_r}(t)\right) = \frac{\pi\alpha P_{LS} R_{ph} G \varepsilon \gamma_r}{6}\left\{p + qe^{-\frac{\pi\gamma_r}{\mathrm{FSR}}}\cos\left[\frac{2\pi}{\mathrm{FSR}}\left(\lambda_r + \widetilde{\delta\lambda_r}(t)\right) + \varphi_i + \psi_e\right]\right\}. \quad (8)$$

Optics EXPRESS

The procedure to arrive at Eq. (8) is similar to the one in [14], but simpler, as a result of using the drop-port transmission and the wide FBG bandwidth. The cosine in Eq. (8) has $2\pi\delta_0 \sin(2\pi f_0 t)/\mathrm{FSR}$ in its argument, leading to Bessel function expansions and harmonics of frequency f_0 [23]. The final result is that the cosine equals a linear combination of an expansion in even harmonics and an expansion in odd harmonics. The prefactors of the expansions are $\cos(2\pi\lambda_r/\mathrm{FSR} + \varphi_i + \psi_e)$ and $\sin(2\pi\lambda_r/\mathrm{FSR} + \varphi_i + \psi_e)$, respectively. In addition, a DC term is part of the expansion in even harmonics, which as a result of the above prefactor depends on φ_i. The DC term and the term p in Eq. (8) add up to the total DC signal contribution to $V_i\left(\widetilde{\delta\lambda}_r(t)\right)$.

Using the values of φ_i, two mutual orthogonal voltages V_x and V_y can be calculated from the V_i:

$$V_x(t) = 2V_1 - V_2 - V_3 = \frac{\pi\alpha P_{LS} R_{ph} G\varepsilon\gamma_r q}{2} e^{-\frac{\pi\gamma_r}{\mathrm{FSR}}} \cos\left[\frac{2\pi}{\mathrm{FSR}}\left(\lambda_r + \widetilde{\delta\lambda}_r(t)\right) + \psi_e\right], \tag{9}$$

$$V_y(t) = \sqrt{3}\,(V_3 - V_2) = \frac{\pi\alpha P_{LS} R_{ph} G\varepsilon\gamma_r q}{2} e^{-\frac{\pi\gamma_r}{\mathrm{FSR}}} \sin\left[\frac{2\pi}{\mathrm{FSR}}\left(\lambda_r + \widetilde{\delta\lambda}_r(t)\right) + \psi_e\right]. \tag{10}$$

The phase modulation $\Phi(t)$ induced by the acoustic waves can be retrieved from V_x and V_y using the arctangent function:

$$\Phi(t) = \tan^{-1}\left(\frac{V_y}{V_x}\right) = \Phi_0 \sin(2\pi f_0 t) + \Delta\Phi\,. \tag{11}$$

Here $\Phi_0 = 2\pi\delta_0/\mathrm{FSR}$ is the phase-modulation amplitude and $\Delta\Phi = 2\pi\lambda_r/\mathrm{FSR} + \psi_e$ is a phase offset.

Eqs. (8)-(11) suggest the following interrogation procedure. First, for a known ultrasound pressure applied to the sensor, time traces of the signals $V_i(t)$ are measured. Then, from these the orthogonal voltages $V_x(t)$ and $V_y(t)$ are constructed, leading to the phase modulation $\Phi(t)$. Applying fast Fourier transform (FFT) to $\Phi(t)$ leads to $\Phi_0 = 2\pi\delta_0/\mathrm{FSR}$, from which finally δ_0 is obtained.

3.2. Matching of the MediGator and the ring-resonator sensor

The MediGator should be sensitive enough to detect a resonance-wavelength modulation below 1 pm. Given $\Phi_0 = 2\pi\delta_0/\mathrm{FSR}$, a smaller FSR of the MZI leads to a higher phase modulation, i.e., a higher sensitivity. However, due to the exponential prefactor of the cosine in Eq. (8), the oscillatory part of V_i strongly decreases with decreasing FSR. To answer the question of the optimum matching of the MediGator and the RR sensor or equivalently the combination of FSR and γ_r giving the maximum signal, we consider the FSR dependence of the sensitivity of V_i to small changes of λ_r, i.e., the function

$$S = \left|\frac{\partial V_i}{\partial\lambda_r}\right| = \frac{\pi\alpha P_{LS} R_{ph} G\varepsilon\gamma_r q}{6} \frac{2\pi}{\mathrm{FSR}} e^{-\frac{\pi\gamma_r}{\mathrm{FSR}}} \left|\sin\left(\frac{2\pi}{\mathrm{FSR}}\lambda_r + \varphi_i + \psi_e\right)\right|. \tag{12}$$

To find the optimum FSR, we apply the condition $\partial S/\partial(\mathrm{FSR}) = 0$. In this, we treat the sine function in Eq. (12) as a constant. This makes sense, since considering the FSR dependence of $|\partial V_i/\partial\lambda_r|$ [effectively done when considering $\partial S/\partial(\mathrm{FSR})$] should not be affected by a changing argument of the sine. Thus, the phase offset $\Delta\Phi = 2\pi\lambda_r/\mathrm{FSR} + \psi_e$ is constant or λ_r keeps pace with a change of FSR, such that λ_r remains at the same phase position of $T_{\mathrm{MZI},i}$. The condition $\partial S/\partial(\mathrm{FSR}) = 0$ then readily leads to the matching condition $\mathrm{FSR} = \pi \times \gamma_r$. For $\gamma_r \approx 100\,\mathrm{pm}$ (typical value of our RRs), this implies an optimum FSR of about 314 pm.

To gain further insight in the signals $V_i(t)$ given by Eq. (8) and their FSR dependence, we performed calculations using MATLAB [24]. We first calculate time traces $V_i(t)$, using the input

Optics EXPRESS

parameters $p = q = 1$, $\lambda_r = 1550\,\text{nm}$, $\gamma_r = 100\,\text{pm}$, $\delta_0 = 35\,\text{pm}$, $f_0 = 1\,\text{MHz}$ and $\text{FSR} = \pi \times \gamma_r$ (optimum matching). Fig. 3(a) shows traces $V_i(t)$. To obtain these $V_i(t)$ traces, we choose ψ_e in the argument of the cosine of Eq. (8) such that a minimum of $T_{\text{MZI},1}(\lambda)$ coincides with λ_r, or equivalently that $\sin(2\pi\lambda_r/\text{FSR} + \varphi_1 + \psi_e) = 0$. This is close to the real case in the interrogation experiments reported below. V_2 and V_3 in this situation are the strongest signals of equal strength, both for the DC and AC component. The latter component has a period of 1 µs, corresponding to the ultrasound frequency f_0. V_1 is dominated by frequency $2f_0$, in agreement with the Bessel function expansions of the cosine in Eq. (8) and the resonance coinciding with a minimum of $T_{\text{MZI},1}(\lambda)$.

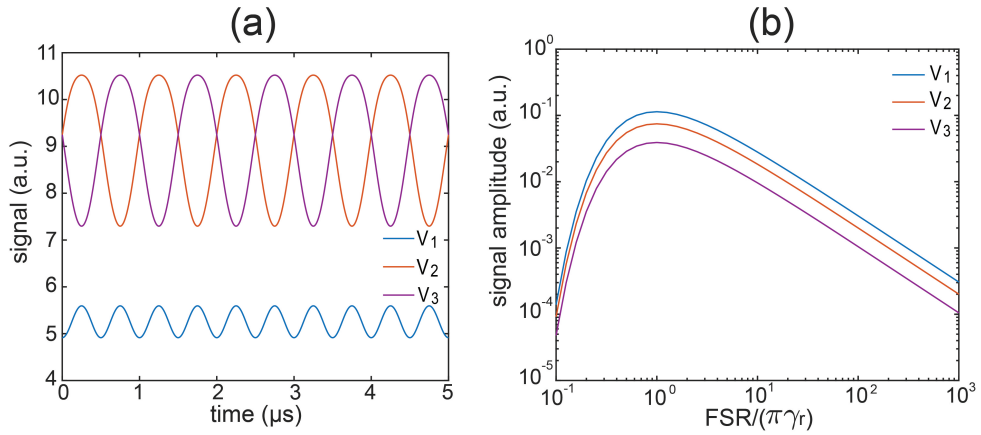

Fig. 3. Calculated output signals of the MediGator, for the interrogation situation specified in the text. (a) Output signals V_i in the time domain. Signal V_1 is dominated by the 2nd harmonic of the ultrasound frequency f_0 due to the alignment of the RR resonance wavelength to a minimum of the MZI transmission at output 1. (b) Amplitude of the signals V_i as a function of the dimensionless ratio $\text{FSR}/(\pi\gamma_r)$. The signal amplitude cannot be directly compared with the signal magnitude in (a) in view of the much weaker modulation amplitude.

The FSR dependence of the oscillatory component of V_i is obtained from traces as in Fig. 3(a), by calculating from these the amplitude as a function of FSR, in this case for $\delta_0 = 1\,\text{pm}$, the required detection limit. In the sweep of FSR, we again maintain a constant phase offset $\Delta\Phi = 2\pi\lambda_r/\text{FSR} + \psi_e$. The other parameters are kept as above. We calculate the FSR dependence for 30 random values of $\Delta\Phi$ in the range $[0, 2\pi]$ using MATLAB, to check whether the general behavior of the FSR dependence depends on $\Delta\Phi$. This turns out to not be the case. A typical result is presented in Fig. 3(b), for $\Delta\Phi = 100.26°$. The maximum of the three curves occurs for $\text{FSR}/(\pi \times \gamma_r) = 1$, in agreement with the above analytical result for optimum matching. It follows that in practice a deviation from optimum matching should be weak in view of the strong FSR dependence of the amplitude of V_i, in particular for FSR values below the one for optimum matching.

4. Characterization of the ring-resonator sensor, the light source and the Mach-Zehnder interferometer

Using the characteristics of the fabricated RR sensor, we arrived at the final design of the MZI and the light source and then fabricated these MediGator components, of which we present the characterization.

Optics EXPRESS

The sensor is characterized from its optical transmission without applied ultrasound, by sweeping the wavelength of a tunable laser (Santec, TSL-550, output power 0.5 mW, step size 5 pm) coupled to the sensor input and by measuring the output power at the sensor drop port with a photodetector (Newport, 1811-FC-AC). Between the laser and the sensor a polarization controller (Thorlabs, FPC562) is used to set the optimum polarization for the grating coupler. In Fig. 4(a) the resulting normalized transmission of the peak centered at 1550.755 nm is plotted (this peak is used in the interrogation experiments below), along with a fit of Eq. (2) to the data points. The fit describes the measured transmission very well, leading to $\gamma_r = 108.17$ pm. The FSR of the RR sensor is 5.02 nm.

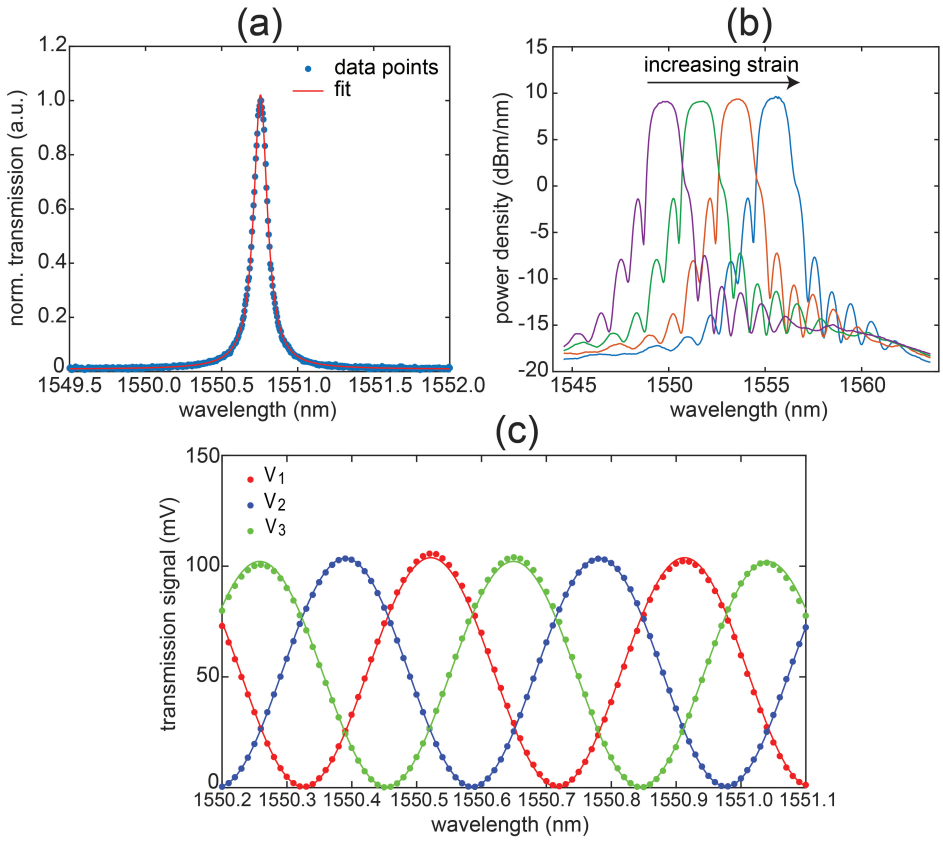

Fig. 4. (a) Transmission peak of the RR sensor. The red curve is a fit of Eq. (2) to the data points. (b) Emission spectra of the MediGator light source. Straining of the FBG results in the observed red shift of the spectra, i.e., the source is tunable. The spectra have a -3 dB bandwidth of 1.5 nm and a maximum power density of 9 dBm/nm. The tuning range shown is 5.7 nm. (c) MZI transmission spectra of the three outputs V_i. The continuous curves are fits of Eq. (5) to the experimental data, giving $\varphi_i = 0°$, 121.1° and 242.7° (i = 1, 2, 3).

Output spectra of the light source for a drive current of the pump laser of 600 mA (interrogation conditions), measured with an OSA (Anritsu, MS9710C), are presented in Fig. 4(b) as a function of the strain applied to the FBG. The measured spectra have a rather flat top, decay steeply and show side lobes characteristic of the FBG reflection spectrum. The power density and the spectral shape are virtually strain independent. The maximum power density is approximately 9 dBm/nm, about one order of magnitude higher than for a high end superluminescent diode emitting around

Optics EXPRESS

1550 nm [25]. The −3 dB bandwidth of the spectra is 1.5 nm, large compared to $\gamma_r = 108.17$ pm and to changes of resonance positions of a silicon RR due to typical environmental temperature variations occurring at a rate of about 80 pm/K [5]. This ensures robust alignment of the source spectrum to the resonance and a wide range of applicable resonance-wavelength modulations. In addition, the bandwidth is smaller than the FSR of the sensor. In Fig. 4(b) we demonstrate a tuning range of the source spectrum of 5.7 nm. This exceeds the FSR of the sensor. The characteristics of the light source make it very suitable for actuating the sensor in the interrogation situation.

The MZI is characterized from its transmission as well, also using the tunable laser and external polarization controller to set the polarization for the PIC, which supposes TE polarization. The three output voltages V_i of the MediGator are sampled using a data acquisition system (based on National Instruments NI 5734, max. sampling rate 120 MSa/s). We find that the acquisition system has stable DC offsets and the MediGator generates constant DC voltages (offsets). These would be added to the DC components of the real signal. We calibrate the DC offsets and subtract these from the measured transmission signals. This leads to the transmission functions in Fig. 4(c), which at first glance show an approximately 120° phase difference. This is confirmed by the phases $\varphi_i = 0°$, 121.1° and 242.7° ($i = 1, 2, 3$) extracted from the fits of Eq. (5) to the measured transmission data, which are plotted in Fig. 4(c) as well. The three outputs each have a fringe visibility of 0.99.

From the transmission data we find that FSR=391.2 pm, to be compared with the design value $\pi \times \gamma_r = 340$ pm. We attribute the difference to fabrication variations. The ratio $\mathrm{FSR}/(\pi \times \gamma_r)$ is 1.15, implying only a slight deviation from the optimum in Fig. 3(b).

From transmission measurements of the MZI we find that its stability, judged from wavelength drift of the transmission curves, amounts to 5 pm in a one hour time period in the stable lab environment. This high stability results from temperature control with the TEC. The temperature control also yields negligible drift of the three DC signals resulting from the MZI transmission drift. These properties enable long time measurements with the MediGator.

5. Experiments with the MediGator

5.1. Measurement of the frequency response of the sensor

For interrogation experiments, the frequency response of the sensor should be known. We measure the frequency response using time-delay spectrometry [26]. We use the interrogator setup of Fig. 2, but replace the data acquisition system and arbitrary waveform generator (AWG) by a frequency spectrum analyzer (FSA, Rigol, DSA815-TG) and its tracking generator, respectively. The sensor and a transducer (Olympus, V314-SU) are coaxially mounted 240 mm apart on the opposite sides of a U-shaped frame in a water tank (see Fig. 2), giving a normal incidence of ultrasound onto the sensor. Using the OSA we align the light-source spectrum to the resonance peak by tuning the FBG and then couple the sensor drop port to the MZI via a polarization controller.

The tracking generator drives the transducer with a sine wave that is swept in frequency and the MediGator signals V_i are sequentially measured by the FSA. The bandwidth filter of the FSA (width 3 kHz) is swept at the same rate as the drive voltage, taking into account the time delay of the acoustic waves between the transducer and the sensor. The frequency is swept from 0.5 MHz to 1.5 MHz. For each V_i we average 50 individual frequency sweeps to obtain the final results, which still include the transducer's frequency characteristic. From these we choose the result for output 3, which gives the highest signal. Among the three outputs, output 3 is closest to the maximum sensitivity according to Eq. (12). The maximum resonance-modulation amplitude is 2.5 pm. By using such small modulation, the second harmonic in V_3 is negligible, which ensures an accurate measurement. We measure the transducer's frequency characteristic using a hydrophone (Precision Acoustics, 1 mm) and correct for it, to obtain the normalized

Optics EXPRESS

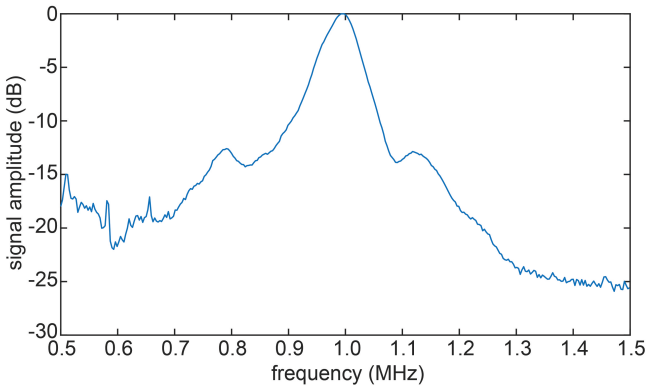

Fig. 5. The normalized frequency response of the RR sensor, giving the resonance frequency of 0.995 MHz.

frequency response of the sensor presented in Fig. 5. The frequency response has its maximum at 0.995 MHz, the frequency of the membrane's lowest vibrational mode. The −6 dB bandwidth, defined as the FWHM of the frequency response divided by the membrane fundamental resonance frequency, is 10.0%.

5.2. *Interrogation experiments*

For the interrogation experiments, we use the complete setup in Fig. 2. First, the pressure of acoustic waves emitted by the transducer, driven by the AWG (Rigol, DG1022), is calibrated using the hydrophone. As in Section 5.1, the light-source spectrum is aligned to the sensor resonance. Then, acoustic waves of frequency $f_0 = 0.995$ MHz, the resonance frequency of the membrane, are sent to the sensor. In this situation traces $V_i(t)$ are measured, using a sampling frequency and measurement time of 30 MHz and 50 ms, respectively. The traces are post-processed using the offset subtraction and noise reduction. For noise reduction we use Gaussian bandpass filters of 100 Hz FWHM and centered at frequency $f_0 = 0.995$ MHz and its harmonics. Examples of time traces $V_i(t)$ are presented in Fig. 6(a), for an ultrasound pressure of 442.4 Pa. The measured traces $V_i(t)$ are close to the calculated traces in Fig. 3(a). Compared to the case of Fig. 3(a), the RR resonance is located slightly to the right of the minimum of $T_{\mathrm{MZI},1}$, which gives V_3 a larger amplitude but a lower DC component compared to V_2. The high degree of resemblance of the measured and calculated traces indicates that the interrogator and the interrogation procedure work as predicted. From the $V_i(t)$ we obtain V_x and V_y plotted in Fig. 6(b). In V_x the second harmonic is also clearly visible. From V_x and V_y and using Eq. (11), we extract $\delta_0 = 34.2$ pm for this pressure.

In Fig. 6(c) the Fourier transform spectra of $V_i(t)$ are presented for a pressure of 1.47 Pa, the lowest pressure used. Even at this pressure, signal spikes at 0.995 MHz about two times higher than the noise floor are clearly discernible in the transforms of V_2 and V_3, which is enough to extract the resonance-modulation amplitude. The signal in the transform of V_1 is below the noise level. The smallness of the latter signal is explained from the resonance wavelength being close to a minimum of $T_{\mathrm{MZI},1}$, as indicated before. In that case, according to Eq. (12) the signal amplitude of V_1 is very close to zero. The $V_i(t)$ for 1.47 Pa yield $\delta_0 = 126$ fm. This value and the S/N ratio of about two indicate that the MediGator is capable of detecting a modulation amplitude down to 100 fm.

Finally, we determine the sensitivity of the sensor, defined as $\partial\delta_0/\partial P$, where P is the pressure of the incident ultrasound. The sensitivity is obtained by interrogating the sensor for 24 pressures

Optics EXPRESS

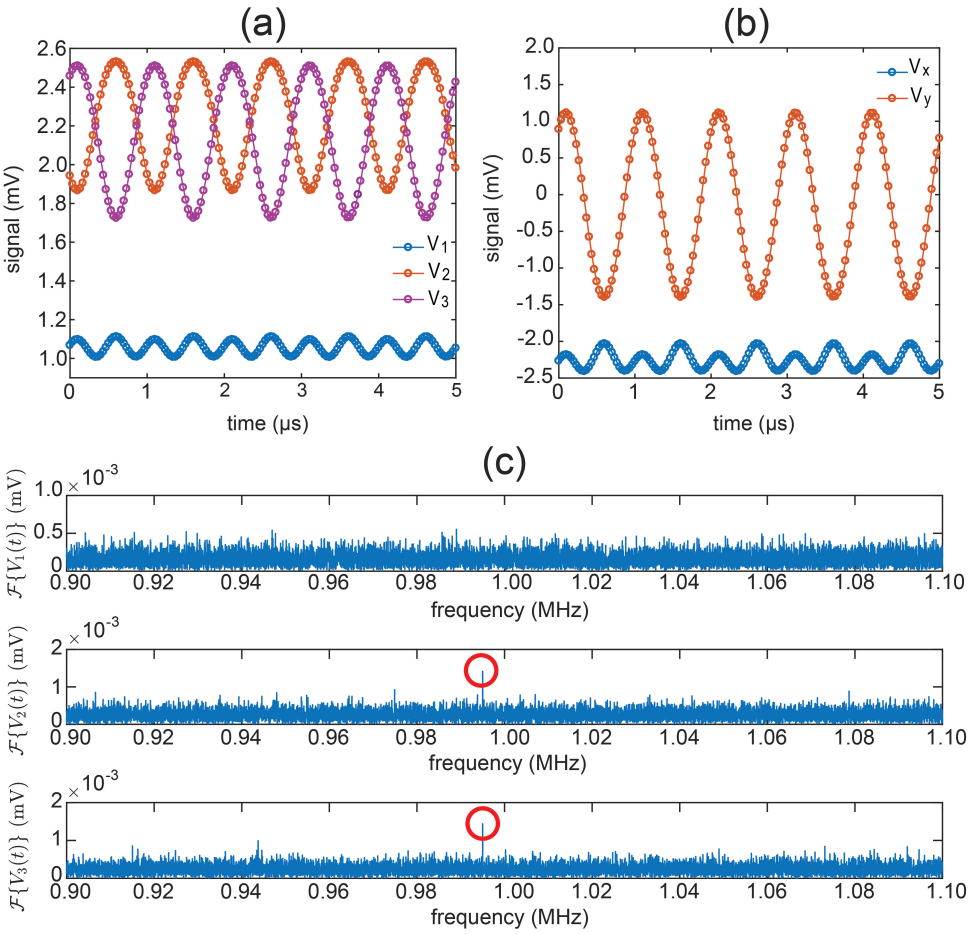

Fig. 6. (a) Measured output signals V_i when interrogating the RR sensor. The applied pressure amplitude is 442.4 Pa. A strong 2nd harmonic is observed in V_1. (b) V_x and V_y as a function of time, calculated from V_i in (a). (c) Fourier transform of the three V_i for a pressure amplitude of 1.47 Pa. For V_2 and V_3, spikes at the ultrasound frequency 0.995 MHz clearly stand out of the noise floor at this low pressure.

Optics EXPRESS

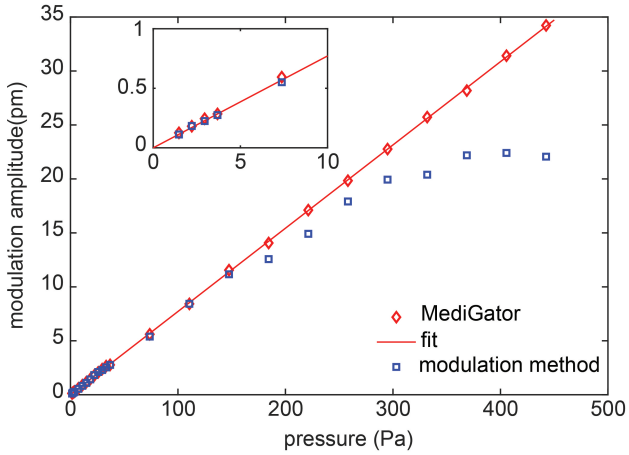

Fig. 7. Amplitude of the resonance-wavelength modulation of the sensor as a function of the ultrasound pressure, measured with the MediGator. The inset zooms in on the low pressure range. The line is a linear fit to the MediGator data points. Its slope is the sensitivity, which amounts to 77.2 fm/Pa. For reference, results obtained with the modulation method are presented as well. The modulation method only agrees with the MediGator approach below 150 Pa. Above this value the modulation method increasingly underestimates the resonance-wavelength modulation.

in the range 1.47 – 442.4 Pa and determining the related δ_0 values. The results are plotted in Fig. 7, along with a linear fit to the data points. The plot shows excellent linearity of the relation between the pressure and the modulation amplitude across the whole pressure range. The slope of the fitted line is 77.2 fm/Pa, which is the sensitivity. For comparison, we also determine the sensitivity using the modulation method explained in Section 1, for which the results are shown in Fig. 7 as well. Very good agreement of the two methods is found for pressures below 150 Pa, leading to the same sensitivity value for both methods. Above 150 Pa, however, the modulation-method points lie increasingly below the MediGator points. This limitation of the modulation method arises from the short linear flank of the transmission peak. We emphasize that the MediGator does not have this limitation, leading to high quality interrogation up to the highest pressure used here, which is not limited by the MediGator itself.

6. Conclusion and outlook

We designed, fabricated and demonstrated an integrated photonics interrogator, called MediGator, for interrogating a ring-resonator (RR) ultrasound sensor. The MediGator comprises i) a novel light source with proper bandwidth around 1550 nm, high power density and large tuning range and ii) an InP Mach-Zehnder interferometer (MZI) with a free spectral range matched to the sensor characteristic. Using its tunable FBG, the light-source spectrum can always be aligned to a single resonance peak of the RR spectrum, the feature for ultrasound sensing. The sensor in the present interrogation demonstration has a 84 µm × 84 µm square membrane, on which the RR is located, and works in the MHz range. Our mathematical description of the signal flow in the MediGator and sensor, apart from yielding matching of the MediGator to the sensor for maximum MZI outputs, leads to the interrogation procedure applied in the experiments. Thanks to the small size of the integrated photonics MZI with the 3 × 3 MMI output and photodetectors, its temperature

Optics EXPRESS

can be accurately regulated during long-time measurements for avoiding environmental phase drift, an issue of our previous fiber MZI based interrogator.

Using the MediGator, we obtain the sensor's acoustic frequency response, giving a resonance frequency of 0.995 MHz and a −6 dB bandwidth of 10.0%. Interrogation experiments show high MediGator performance, reflected in ease of aligning the light source to the RR resonance and high linearity of the plot of applied acoustic pressure versus resonance-wavelength modulation. This results in a sensitivity of 77.2 fm/Pa of the sensor. The minimum ultrasound pressure detected is 1.47 Pa, resulting after FFT of the measured signals. Compared to the modulation method, the MediGator exhibits a three times larger measurement range, which in the experiments is limited by the highest applied pressure and not by the MediGator itself. In spite of one MediGator output signal accidentally being rather close to zero as a result of the wavelength position of resonance peak, the MediGator operates very well, underlining the strength of using a 3×3 MMI at the MZI output. Summarizing, the primary merits of the MediGator are ease of operation, temperature robustness, low detection limit, large measurement range, compactness and cost effective, making the instrument very suitable for interrogating the RR ultrasound sensor.

Further improving the S/N ratio and enabling even lower detection limit are possible through several methods: improving the fiber-chip coupling, adding second-stage amplifiers after the TIAs, and further shielding of the MediGator for noise from the environment. We envision that real-time interrogation of the RR ultrasound sensor can be realized by implementing real-time signal filtering and processing to obtain the resonance-wavelength modulation. In addition, the architecture of the MZI chip can be adapted for interrogating an array of RR sensors by adding arrayed waveguide gratings or cascaded MZIs for multiplexing and demultiplexing [27, 28]. Finally, we note that owing to the temperature stabilization of the crucial parts of the MediGator, it can also interrogate RR sensors (not limited silicon ones) for sensing of signals slower than induced by ultrasound waves. This makes the MediGator highly versatile.

Funding

Nederlandse Organisatie voor Wetenschappelijk Onderzoek (NWO) (13534).

Acknowledgments

The authors thank the Kavli Nanolab Delft for the fabrication support, S. Verstuyft for thinning down the SOI chips, L. Orbe and E. Wan for valuable discussions, and W. J. Westerveld for designing the ring resonator.

References

1. N. A. Yebo, P. Lommens, Z. Hens, and R. Baets, "An integrated optic ethanol vapor sensor based on a silicon-on-insulator microring resonator coated with a porous ZnO film," Opt. Express **18**, 11859–11866 (2010).
2. M. Boerkamp, T. van Leest, J. Heldens, A. Leinse, M. Hoekman, R. Heideman, and J. Caro, "On-chip optical trapping and Raman spectroscopy using a TripleX dual-waveguide trap," Opt. Express **22**, 30528–30537 (2014).
3. K. De Vos, I. Bartolozzi, E. Schacht, P. Bienstman, and R. Baets, "Silicon-on-insulator microring resonator for sensitive and label-free biosensing," Opt. Express **15**, 7610–7615 (2007).
4. P. V. Lambeck, "Integrated optical sensors for the chemical domain," Meas. Sci. Technol. **17**, R93–R116 (2006).
5. G.-D. Kim, H.-S. Lee, C.-H. Park, S.-S. Lee, B. T. Lim, H. K. Bae, and W.-G. Lee, "Silicon photonic temperature sensor employing a ring resonator manufactured using a standard CMOS process," Opt. Express **18**, 22215–22221 (2010).
6. H. Xu, M. Hafezi, J. Fan, J. M. Taylor, G. F. Strouse, and Z. Ahmed, "Ultra-sensitive chip-based photonic temperature sensor using ring resonator structures," Opt. Express **22**, 3098–3104 (2014).
7. B. Ouyang, Y. Li, M. Kruidhof, R. Horsten, K. W. van Dongen, and J. Caro, "On-chip silicon Mach-Zehnder interferometer sensor for ultrasound detection," Opt. Lett. **44**, 1928–1931 (2019).
8. A. Rosenthal, M. Omar, H. Estrada, S. Kellnberger, D. Razansky, and V. Ntziachristos, "Embedded ultrasound sensor in a silicon-on-insulator photonic platform," Appl. Phys. Lett. **104**, 021116 (2014).

Optics EXPRESS

9. S. Leinders, W. Westerveld, J. Pozo, P. Van Neer, B. Snyder, P. O'Brien, H. Urbach, N. De Jong, and M. Verweij, "A sensitive optical micro-machined ultrasound sensor (OMUS) based on a silicon photonic ring resonator on an acoustical membrane," Sci. Rep. **5**, 14328 (2015).
10. A. Maxwell, S.-W. Huang, T. Ling, J.-S. Kim, S. Ashkenazi, and L. J. Guo, "Polymer microring resonators for high-frequency ultrasound detection and imaging," IEEE J. Sel. Topics Quantum Electron. **14**, 191–197 (2008).
11. C. Zhang, S.-L. Chen, T. Ling, and L. J. Guo, "Review of imprinted polymer microrings as ultrasound detectors: Design, fabrication, and characterization," IEEE Sensors J. **15**, 3241–3248 (2015).
12. T. Claes, J. G. Molera, K. De Vos, E. Schacht, R. Baets, and P. Bienstman, "Label-free biosensing with a slot-waveguide-based ring resonator in silicon on insulator," IEEE Photon. J. **1**, 197–204 (2009).
13. N. A. Yebo, W. Bogaerts, Z. Hens, and R. Baets, "On-chip arrayed waveguide grating interrogated silicon-on-insulator microring resonator-based gas sensor," IEEE Photon. Technol. Lett. **23**, 1505–1507 (2011).
14. F. G. Peternella, B. Ouyang, R. Horsten, M. Haverdings, P. Kat, and J. Caro, "Interrogation of a ring-resonator ultrasound sensor using a fiber Mach-Zehnder interferometer," Opt. Express **25**, 31622–31639 (2017).
15. Y. E. Marin, T. Nannipieri, C. J. Oton, and F. Di Pasquale, "Current status and future trends of photonic-integrated FBG interrogators," J. Lightw. Technol. **36**, 946–953 (2018).
16. K. Jansen, A. F. W. van der Steen, H. M. M. van Beusekom, J. W. Oosterhuis, and G. van Soest, "Intravascular photoacoustic imaging of human coronary atherosclerosis," Opt. Lett. **36**, 597–599 (2011).
17. W. J. Westerveld, S. M. Leinders, P. M. Muilwijk, J. Pozo, T. C. van den Dool, M. D. Verweij, M. Yousefi, and H. P. Urbach, "Characterization of integrated optical strain sensors based on silicon waveguides," IEEE J. Sel. Topics Quantum Electron. **20**, 101–110 (2013).
18. ePIXfab, http://epixfab.eu/, accessed on July 15, 2019.
19. C. Castellan, A. Chalyan, M. Mancinelli, P. Guilleme, M. Borghi, F. Bosia, N. M. Pugno, M. Bernard, M. Ghulinyan, G. Pucker, and L. Pavesi, "Tuning the strain-induced resonance shift in silicon racetrack resonators by their orientation," Opt. Express **26**, 4204–4218 (2018).
20. W. Bogaerts, P. De Heyn, T. Van Vaerenbergh, K. De Vos, S. Kumar Selvaraja, T. Claes, P. Dumon, P. Bienstman, D. Van Thourhout, and R. Baets, "Silicon microring resonators," Laser Photonics Rev. **6**, 47–73 (2012).
21. A. Escuer, S. Jarabo, and J. Álvarez, "Experimental validation of the improved analytical model for erbium-doped fibre lasers based on the energy conservation principle," Appl. Phys. B **81**, 831–840 (2005).
22. SMART Photonics, https://smartphotonics.nl/, accessed on July 15, 2019.
23. F. W. J. Olver, "Bessel functions of integer order," in *Handbook of Mathematical Functions with Formulas, Graphs and Mathematical Tables*, M. Abramowitz and I. A. Stegun, eds. (Dover books on Mathematics, 1964).
24. MATLAB R2017a, The MathWorks, Inc., Natick, Massachusetts, United States.
25. EXALOS, "SLED Modules," http://www.exalos.com/sled-modules/, accessed on May 20, 2019.
26. R. A. Smith and D. R. Bacon, "A multiple-frequency hydrophone calibration technique," J. Acoust. Soc. Am. **87**, 2231–2243 (1990).
27. M. K. Smit and C. Van Dam, "PHASAR-based WDM-devices: Principles, design and applications," IEEE J. Sel. Topics Quantum Electron. **2**, 236–250 (1996).
28. F. Horst, W. M. Green, S. Assefa, S. M. Shank, Y. A. Vlasov, and B. J. Offrein, "Cascaded Mach-Zehnder wavelength filters in silicon photonics for low loss and flat pass-band WDM (de-) multiplexing," Opt. Express **21**, 11652–11658 (2013).

131.180.131.188{ts'2019-08-19 04:12:01'}